Computational and Theoretical Chemistry 1257 (2026) 115682

Contents lists available at ScienceDirect

Computational and Theoretical Chemistry

journal homepage: www.elsevier.com/locate/comptc

The reactive fingerprint of toxic alkylphenols: Insights from NO^+ chemical ionization and spectroscopy

Manjeet Bhatia

QuantumSIMM, Kangra, Himachal Pradesh, 177105, India

ARTICLE INFO

Keywords:
Mass spectrometry
DFT
Hybrid functional
Spectroscopy
Endocrine disruptors
Collision rates

ABSTRACT

Alkylphenols, which consist of a phenolic ring attached to an alkyl chain, are widely used in industrial processes and consumer products, including food-contact materials such as plastic containers. Their broad application raises concerns regarding human exposure and environmental impact. In this work, density functional theory (DFT) was employed to investigate the electronic structure and chemical reactivity of alkylphenols using different DFT functionals. The key molecular descriptors, including ionization energy, electron affinity, HOMO–LUMO gap, and global reactivity parameters, were systematically evaluated. Excited-state properties and UV–Vis absorption spectra were further examined through time-dependent DFT (TD-DFT). The potential of NO^+ as a reagent ion was also explored through charge transfer and H^- abstraction reactions. Benchmark DFT calculations confirm that B3LYP/6-311++G(d, p) is well-suited for ground-state studies, and further evaluations demonstrate that NO^+ readily undergoes exothermic charge transfer with alkylphenols, proceeding at collision-controlled rates. In contrast, hydride abstraction is endothermic, and association pathways are not favorable. These findings underscore the potential of NO^+-based chemical ionization mass spectrometry (CIMS) techniques, such as PTR-MS and SIFT-MS, for the sensitive detection and quantification of alkylphenols. Overall, this comprehensive computational study provides valuable insights into the stability, reactivity, and photophysical behavior of alkylphenols, advancing their identification in both environmental monitoring and human health risk assessments.

1. Introduction

Alkylphenols have garnered significant attention due to their widespread presence in the environment and their potential role as endocrine disruptors and xenoestrogens [1,2]. These compounds serve as key raw materials in the production of various industrial products, including surfactants, detergents, phenolic resins, polymer additives, and lubricants. However, their hazardous nature classifies them among the most concerning environmental toxicants, primarily due to their endocrine-disrupting effects [3,4]. Among alkylphenols, octylphenol and nonylphenol are capable of binding to estrogen receptors, thereby disrupting the endocrine system. In addition to its use in the production of nonylphenol ethoxylates — nonionic surfactants and detergents — nonylphenol is also widely employed as an intermediate in the polymer industry for the manufacture of resins, plastics, and stabilizers, as well as in the production of mineral ore extraction chemicals such as phenolic oximes [5,6]. Nonylphenol ethoxylates are commonly used in laundering and cleaning applications, including floor and surface cleaning in buildings, vehicle cleaning, antistatic formulations, and metal cleaning [7]. Further applications extend to textile manufacturing and leather processing, agriculture, emulsion polymerization, and the production of paints and lacquers [7,8].

The main emission pathways of alkylphenols include wastewater effluent (wastewater treatment plant discharge), industrial site release, and land application of sewage sludge/biosolids, which are repeatedly identified as primary environmental inputs. These compounds persist in sediments, biota, and soils where alkylphenol ethoxylates have been used. Their release into the environment can lead to estrogenic activity and reproductive toxicity, interfering with the endocrine system in both humans and animals [9].

Recent advances in real-time chemical ionization mass spectrometry (CIMS) methods, proton transfer reaction mass spectrometry (PTR-MS), and selected ion flow tube mass spectrometry (SIFT-MS) have enabled high-sensitivity, non-destructive detection of alkylphenols at trace levels in air, water, and biological matrices [10,11]. These methods offer advantages over GC–MS and LC–MS, especially for volatile or semi-volatile organic compounds, by avoiding sample preparation and reducing analysis time. Research highlights the urgent need for

E-mail address: manjeet.bhatia@quantumsimm.com.
URL: http://www.quantumsimm.com.

https://doi.org/10.1016/j.comptc.2026.115682
Received 28 October 2025; Received in revised form 12 January 2026; Accepted 13 January 2026
Available online 15 January 2026

environmental monitoring of alkylphenols due to their persistence, bioaccumulation, and contribution to ecosystem and health risks.

Theoretical studies of the toxicological, chemical reactivity, and optical absorption properties of alkylphenols, along with their fundamental electronic-structure parameters, are essential for effective environmental monitoring, their identification and quantification through CIMS techniques. Density Functional Theory (DFT) has been widely recognized as a powerful computational approach for analyzing the chemical and reactivity properties of organic compounds [12–14].

Most previous studies on alkylphenols focus on isolated aspects such as, environmental occurrence and toxicity, biodegradable or fate in aquatic systems, and targeted analytical detection using GC–MS or LC–MS [15–17]. Very few studies attempt a holistic molecular level characterization that systematically addresses electronic structure, spectroscopy, and ionization chemistry [18,19]. However, electronic structure and reactivity analysis of alkylphenols are scarce, especially comparative trends across different alkylphenols and different DFT functionals.

However, detailed electronic structure and reactivity analyses of alkylphenols remain limited; the existing data on alkylphenols often contain significant uncertainties, as the presence of large alkyl chains increases the computational cost of DFT calculations and introduces substantial conformational flexibility. Variations in chain folding and orientation can strongly influence molecular properties such as polarizability. This means a single optimized geometry may not adequately represent the ensemble-averaged behavior [18,20,21]. In addition, ionization energies are ideally determined experimentally using photoelectron spectroscopy; however, for larger alkylphenols, such measurements are scarce or unavailable and may be complicated by thermal decomposition, molecular alignment effects, or experimental limitations.

The present study fills this gap by providing qualitative descriptors that explain structure–reactivity relationships. To ensure accurate and reliable computations, a benchmark study is conducted using time-dependent DFT (TD-DFT) with eight different DFT functionals and the 6-311++G(d, p) basis set to evaluate the most suitable method for predicting the excited-state properties of alkylphenols. [22–24]. By integrating quantum chemistry, spectroscopy, and real-time mass spectrometry, this work advances beyond descriptive environmental studies and establishes a predictive framework for understanding the behavior of alkylphenols in atmospheric and analytical contexts.

2. Computations

This study employs various DFT functionals in combination with the 6-311++G(d, p) basis set to optimize the molecular structures of alkylphenols. All computations were carried out using the Gaussian 16 software suite [25]. The optimized structures were confirmed as true minima by ensuring the absence of imaginary frequencies in the vibrational analysis. Electronic excited-state calculations were performed on the optimized geometry using the TDDFT method. TDDFT is an extension of DFT used to study the electronic dynamics of systems under time-dependent external fields [26–28]. It is widely applied to calculate excited-state properties such as optical absorption spectra and electronic excitations in molecules and solids [29].

All calculations were performed for neutral molecules (total charge = 0) in their closed-shell singlet ground state (spin multiplicity = 1). Derived from conceptual DFT, global reactivity descriptors such as chemical potential (μ), chemical hardness (η), softness (σ), and electrophilic index (ω) quantify molecular reactivity using ionization potential (IP) and electron affinity (EA), often approximated via Koopmans' theorem ($IP \approx -E_{HOMO}$, $EA \approx -E_{LUMO}$) [30–33].

These reactivity tools are vital in rationalizing trends in assessing molecular reactivity, catalysis, material science, and drug design [34]. Chemical potential $\mu = -\chi$ (electronegativity, χ) is analogous to the chemical potential in thermodynamics, which is the tendency of a substance to undergo a chemical change. In the context of molecules, it represents the escaping tendency of electrons. μ can be computed using the equation below:

$$\mu = \frac{IE + EA}{2} = -\frac{E_{HOMO} + E_{LUMO}}{2} \quad (1)$$

A more negative μ indicates higher electronegativity and electron-accepting tendency. Chemical hardness η represents the resistance to electron density redistribution.

$$\eta = \frac{IE - EA}{2} = \frac{E_{LUMO} - E_{HOMO}}{2} \quad (2)$$

So the HOMO–LUMO gap is E_{LUMO}-E_{HOMO}, which is equal to 2η. Therefore, the gap is directly related to hardness. A large gap implies a hard molecule, less reactive; a small gap implies soft, more reactive. Then softness (σ) is the inverse of hardness, $1/(2\eta)$.

$$\sigma = \frac{1}{2\eta} = \frac{1}{E_{LUMO} - E_{HOMO}} \quad (3)$$

Softer molecules (smaller gaps) are more reactive and prone to electron redistribution, indicating polarizability. The electrophilic index (ω) is defined as $\frac{\mu^2}{2\eta}$ measures electrophilic strength, which is similar to the concept of electronegativity squared over hardness. That makes sense because a higher electronegativity (related to μ) and lower hardness would mean a higher tendency to attract electrons, hence higher electrophilicity.

$$\omega = \frac{\mu^2}{2\eta} = \frac{(E_{HOMO} + E_{LUMO})^2}{4(E_{LUMO} - E_{HOMO})} \quad (4)$$

Higher ω values indicate stronger electrophiles (high electronegativity, low hardness).

The selected functionals encompass a range of hybrid approaches, including global hybrid functionals, range-separated hybrid functionals, screened hybrid functionals, and HF calculations.

The chosen DFT functionals represent diverse approaches to incorporating exact exchange and correlation effects, balancing computational cost and accuracy:

- Global Hybrid Functionals: B3LYP (Becke 3-parameter, Lee–Yang–Parr Functional) is one of the most widely used functionals. B3LYP incorporates 20% exact HF exchange and 80% generalized gradient approximation (GGA) exchange [35]. It is well-known for its good performance in predicting molecular geometries, vibrational spectra, and electronic properties at a reasonable computational cost. PBE0 (Perdew–Burke–Ernzerhof Hybrid Functional) hybrid functional [36] that combines 25% HF exchange with 75% GGA exchange, while the correlation part is derived entirely from PBE. It is known for its accuracy in both organic and inorganic systems, as well as for solid-state materials. M06-2X [37] is a highly parameterized meta-hybrid functional that includes 54% HF exchange with the remaining 46% coming from the semi-local exchange functional; this percentage applies to both the short-range and long-range interactions as M06-2X does not utilize a range-separation scheme to differentiate between them. It is particularly effective for non-covalent interactions, main-group thermochemistry, and transition metal chemistry.
- Range-Separated Hybrid Functionals: CAM-B3LYP (Coulomb-Attenuated Method B3LYP) functional [38] is a hybrid functional used in computational chemistry, combining a long-range corrected (LC) exchange–correlation term with the popular B3LYP functional. CAM-B3LYP modifies B3LYP by incorporating 19% HF exchange in the short range and 65% in the long range, improving its performance for charge transfer excitations. It is widely used for excited-state calculations and systems with significant electron delocalization. It is commonly used for molecular modeling and quantum chemistry calculations. Similarly, LC-wHPBE (Long-Range Corrected PBE with a wHPBE Exchange Functional) functional [39] applies 0% HF exchange in the short range

and 100% in the long range, making it suitable for long-range interactions, charge transfer complexes, and large biomolecular systems [40,41].

- Screened Hybrid Functionals: HSEH1PBE (Heyd–Scuseria–Ernzerhof Hybrid Functional) functional [42,43] used in DFT calculations, which blends a short-range exchange–correlation functional (PBE) with a portion of exact HF exchange. HSEH1PBE incorporates 25% HF exchange at short range and 0% at long range, which reduces computational cost while maintaining good accuracy for periodic systems and solid-state materials. It is designed to improve the accuracy of electronic structure calculations, particularly for systems with delocalized electrons or excited states. It is particularly effective for band gap predictions and structural properties of materials [44].
- Dispersion-Corrected Range-Separated Hybrid Functionals: wB97XD [45] is a range-separated hybrid functional that includes dispersion correction via empirical terms. It includes long-range exact exchange and an empirical dispersion (D) correction. It applies 22% HF exchange at short range and 100% at long range, making it highly suitable for systems dominated by dispersion forces, such as van der Waals complexes and biomolecules. wB97XD is known for improved accuracy in describing noncovalent interactions, thermochemical properties, and long-range charge-transfer systems.

The 6-311++G(d, p) basis set [46,47] was considered for its balanced treatment of valence and diffuse electron density. It includes triple-zeta split-valence functions to accurately represent core and valence orbitals. Diffuse functions (++) are essential for describing weakly bound systems, anions, and molecules with significant electron delocalization [48]. The polarization functions (d, p) included to enhance the flexibility of molecular orbitals, improving accuracy in describing molecular geometries and interactions [49]. Alternative basis sets involve trade-offs between computational cost and accuracy: 6-31+G(d,p) reduces computational cost but is less suitable for high-precision vibrational analysis, 6-311G(d,p) is adequate for geometry optimization but lacks diffuse functions, and aug-cc-pVTZ offers benchmark-level accuracy at substantially higher computational cost.

The combination of these functionals and basis sets allows for a comprehensive investigation of alkylphenols, covering both ground-state electronic properties and non-covalent interactions. The inclusion of functionals with varying HF exchange contributions enables a comparative analysis of their performance in predicting ionization energy, dipole moments, polarizability, and electronic structure characteristics. The results provide insights into how different functionals capture electron correlation and exchange effects, ultimately aiding in the selection of an optimal functional for future studies on alkylphenols and related organic compounds.

3. Results & Discussions

All molecular structures of alkylphenols were fully optimized using individual DFT functionals with the 6-311++G(d, p) basis set. The optimized geometrical structures are presented in Fig. 1. Table 1 summarizes the computed results, including minimum electronic energy, dipole moment, polarizability, ionization energy (IE), electron affinity (EA), highest occupied molecular orbital (HOMO) and lowest unoccupied molecular orbital (LUMO) energies, and the HOMO–LUMO energy gap for eight different DFT functionals.

3.1. Electronic structure

3.1.1. Reference DFT functional

For 2-EPh, B3LYP was found to yield the lowest electronic energy, while HF resulted in the highest optimization energy. Functionals such as M06-2X and wB97XD produced optimized energies that closely matched those obtained from B3LYP. This trend was consistently observed across all investigated alkylphenols.

The computed electric dipole moment of 2-EPh was found to be 1.38 Debye, aligning well with reported literature values of 1.37 Debye [50], whereas for 4-OPh, it was determined to be 1.53 Debye [51]. Since geometry optimization and ground-state properties are relatively insensitive to the amount of correlation energy and HF exchange included in the functional, the calculated parameters showed only slight variations across different functionals. They were in close agreement with previously reported values.

The IE, which represents the energy required to remove an electron from a molecular system, was found to be 8.14 eV for p-ethylphenol, as per literature [52]. The computed IE values using B3LYP (8.24 eV), HSEH1PBE (8.22 eV), PBE0 (8.23 eV), and wB97XD (8.29 eV) were in close agreement with the reported data. These functionals incorporate 20%–25% exact HF exchange, which contributes to the accuracy of their IE predictions. However, functionals with a higher proportion of exact HF exchange, such as M06-2X and range-separated functionals, which include HF exchange in both short- and long-range interactions, tend to overestimate IE for alkylphenols. A graphical representation of IE at DFT functional is shown in Fig. 2. A similar trend was observed for 2-PPh, where the reported IE value of 8.20 eV [53] was in excellent agreement with B3LYP (8.19 eV), HSEH1PBE (8.17 eV), PBE0 (8.19 eV), and wB97XD (8.21 eV). These results reinforce the reliability of hybrid functionals that incorporate a moderate amount of HF exchange.

Table S3 in the supplementary materials presents the exact HF exchange contributions for various DFT functionals, highlighting their influence on computed electronic properties. The results of this study provide a comprehensive comparison of different DFT functionals for alkylphenol derivatives, demonstrating their effectiveness in accurately predicting molecular properties relevant to their stability and reactivity.

3.1.2. Chemical reactivity via C-DFT

These reactivity descriptors are obtained for 5 alkylphenols via 8 DFT functional and shown in Table 2.

Koopmans' theorem is an approximation and assumes that the orbitals do not relax when electrons are added or removed. In reality, ionization and electron affinity would involve some relaxation, so these values might not be exact. However, approximation is used for these descriptors.

When comparing the computed IE with the HOMO–LUMO energies from various functionals, it is evident that range-separated DFT functionals such as CAM-B3LYP, wB97XD, and LC-wHPBE, along with the global hybrid functional M06-2X, produce comparable results for IE $\approx -\varepsilon_{HOMO}$. Specifically, CAM-B3LYP underestimates IE values by 6%–8%, while LC-wHPBE overestimates IE by less than 6%. Likewise, wB97XD computes IE within 1%–2% of HOMO.

In contrast, the computed EA from these functionals is less accurate, except for B3LYP, PBE0, and HSEH1PBE, which provide a better correlation with EA $\approx -\varepsilon_{LUMO}$. B3LYP overestimates EA for 2-EPh, 2-PPh, and 4-OPh by 9%, 7%, and 18%, respectively, and for 2-NPh and 4-NPh, the overestimation exceeds 30%. Similarly, PBE underestimates EA by about 50%, while HSEH1PBE overestimates EA by 9%–40%, except for 4-OPh, where it underestimates EA by 8%. These results demonstrate that while these values may not be perfectly accurate, they can still be useful for predicting how a molecule will interact in chemical reactions, as well as its stability, reactivity of a molecule, and whether it is more likely to act as an electrophile or nucleophile.

3.2. Spectroscopy

3.2.1. IR spectra

Infrared (IR) spectroscopy is a crucial analytical technique used to identify characteristic absorption peaks corresponding to various functional groups and molecular structures. In this study, the fundamental

Table 1
Computed electronic energy (ΔE_{Min}), dipole moment (μ_D), polarizability (α), ionization energy (IE), electron affinity (EA), HOMO–LUMO energy, and HOMO–LUMO gap (ΔE_G) of alkylphenols with 6-311++G(d, p) basis set.

		2-EPh ($C_8H_{10}O$)	2-NPh ($C_{15}H_{24}O$)	2-PPh ($C_9H_{12}O$)	4-NPh ($C_{15}H_{24}O$)	4-OPh ($C_{14}H_{22}O$)
B_3LYP	ΔE_{Min}	−386.2103323	−661.481111	−425.534994	−661.480409	−622.156066
	μ_D	1.10	1.15	1.14	1.45	1.46
	α	14.46	27.73	16.40	27.83	25.94
	IE	8.24	8.09	8.19	7.98	7.99
	EA	0.44	0.68	0.43	0.30	0.41
	E_{HOMO}	−6.24	−6.22	−6.23	−6.12	−6.12
	E_{LUMO}	−0.48	−0.45	−0.46	−0.50	−0.50
	ΔE_G	5.76	5.77	5.78	5.62	5.62
CAM-B_3LYP	ΔE_{Min}	−385.997276	−661.092786	−425.296893	−661.091620	−621.792312
	μ_D	1.10	1.15	1.17	1.53	1.55
	α	14.47	27.73	16.40	27.83	25.94
	IE	8.33	8.26	8.30	8.14	8.14
	EA	0.62	0.59	0.61	0.59	0.60
	E_{HOMO}	−7.66	−7.64	−7.65	−7.52	−7.52
	E_{LUMO}	0.28	0.28	0.29	0.31	0.31
	ΔE_G	7.95	7.93	7.94	7.83	7.83
HF	ΔE_{Min}	−383.729676	−657.038819	−422.774054	−657.038085	−617.993965
	μ_D	1.13	1.18	1.17	1.53	1.55
	α	13.41	25.47	15.16	25.48	23.76
	IE	7.18	7.12	7.15	7.06	7.07
	EA	0.93	0.87	0.89	0.88	0.88
	E_{HOMO}	−8.46	−8.44	−8.46	−8.31	−8.32
	E_{LUMO}	1.01	1.00	1.01	1.01	1.01
	ΔE_G	9.47	9.45	9.47	9.32	9.33
HSEH1PBE	ΔE_{Min}	−385.778822	−660.723344	−425.056900	−660.722350	−621.444621
	μ_D	1.12	1.17	1.16	1.43	1.44
	α	14.27	27.39	16.18	27.49	25.62
	IE	8.22	8.08	8.17	7.96	7.97
	EA	0.44	0.54	0.44	0.51	0.71
	E_{HOMO}	−6.04	−6.02	−6.03	−5.91	−5.91
	E_{LUMO}	−0.62	−0.59	−0.60	−0.65	−0.65
	ΔE_G	5.43	5.43	5.43	5.26	5.26
LC-wHPBE	ΔE_{Min}	−385.933509	−661.029305	−425.233159	−661.028138	−621.728791
	μ_D	1.14	1.20	1.19	1.51	1.52
	α	13.64	26.04	15.45	26.13	24.36
	IE	8.43	8.36	8.40	8.25	8.25
	EA	0.67	0.65	0.66	1.32	1.32
	E_{HOMO}	−8.91	−8.89	−8.90	−8.75	−8.75
	E_{LUMO}	0.93	0.93	0.93	0.94	0.94
	ΔE_G	9.84	9.81	9.83	9.69	9.69
M06-2X	ΔE_{Min}	−386.034609	−661.159017	−425.338388	−661.157082	−621.393184
	μ_D	1.13	1.19	1.18	1.49	1.50
	α	13.99	26.89	15.87	26.97	25.13
	IE	8.48	8.40	8.44	8.26	8.26
	EA	0.71	0.67	0.74	0.67	0.68
	E_{HOMO}	−7.57	−7.55	−7.56	−7.43	−7.43
	E_{LUMO}	−0.17	−0.18	−0.17	−0.15	−0.15
	ΔE_G	7.41	7.38	7.40	7.28	7.28
PBE0	ΔE_{Min}	−385.746019	−660.668788	−425.020988	−660.667805	−621.393184
	μ_D	1.12	1.17	1.16	1.43	1.44
	α	14.24	27.34	16.15	27.43	25.57
	IE	8.23	8.11	8.19	7.99	8.00
	EA	0.49	0.41	0.48	0.46	0.47
	E_{HOMO}	−6.43	−6.41	−6.42	−6.30	−6.30
	E_{LUMO}	−0.25	−0.22	−0.15	−0.27	−0.27
	ΔE_G	6.18	6.19	6.19	6.03	6.02
wB97XD	ΔE_{Min}	−386.075256	−661.264345	−425.388324	−661.263165	−621.950515
	μ_D	1.12	1.19	1.17	1.46	1.47
	α	14.11	27.02	15.99	27.11	25.27
	IE	8.29	8.21	8.25	8.09	8.09
	EA	0.73	0.71	0.73	0.73	0.73
	E_{HOMO}	−8.19	−8.17	−8.18	−8.04	−8.04
	E_{LUMO}	1.01	1.01	1.01	1.02	1.02
	ΔE_G	9.19	9.17	9.19	9.06	9.06

CAS no: 2-EPh (90-00-6), 2-NPh(136-83-4), 2-PPh(694-35-9), 4-NPh(104-40-5), 4-OPh(1806-26-4).
ΔE_{Min} in Hartree, μ_D in Debye, α in $Å^3$, HOMO–LUMO energy in eV, and ΔE_G in eV.

vibrational modes and their corresponding intensities were computed using eight different DFT functionals combined with the 6-311++G(d, p) basis set. Fig. 3 presents the computed IR spectra for 2-EPh using different DFT functionals. The 2-EPh molecule, consisting of 19 atoms, exhibits 51 fundamental vibrational modes within a C1 point group symmetry.

It should be noted that when two conformers differ due to the presence or absence of intramolecular hydrogen bonding, IR spectroscopy

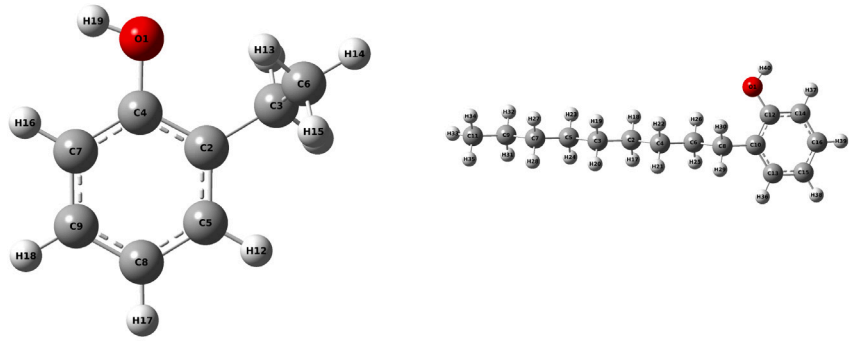

(a) 2-EPh

(b) 2-NPh

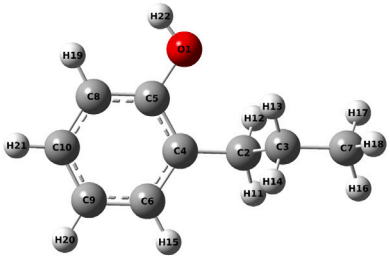

(c) 2-PPh

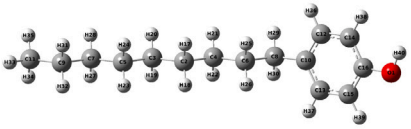

(d) 2-NPh

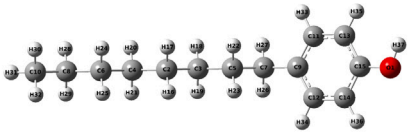

(e) 4-OPh

Fig. 1. Optimized geometries of alkylphenols using B3LYP/6-311++G(d, p) DFT method.

can reveal multiple O–H stretching bands, indicating the coexistence of more than one conformer. The computed IR spectra of 2-EPh exhibit two distinct O–H stretching bands at 3836 cm^{-1} and approximately 3104 cm^{-1}, corresponding to different conformational forms arising from ortho substitution by the ethyl group.

The more stable gauche (cis) conformer is characterized by the orientation of the –OH group toward the ethyl chain, enabling intramolecular hydrogen bonding. This conformer is stabilized by a C–H··· O interaction between the α-hydrogen of the ethyl group and the oxygen atom of the hydroxyl group, resulting in a lower total energy (–386.2103 au). In contrast, the trans conformer, in which the –OH group is oriented away from the ethyl substituent, lacks this stabilizing interaction and is therefore higher in energy (–386.2092 au).

Spectroscopic techniques can distinguish between these conformers because each possesses slightly different energy levels and, consequently, distinct spectral signatures. The hydrogen-bonded O–H stretch of the cis conformer appears as a broadened band at a lower frequency around 3100 cm^{-1}, whereas the free O–H stretching vibration of the trans conformer occurs at the higher frequency of 3836 cm^{-1}.

Additionally, multiple peaks between 1646 cm^{-1} and 1186 cm^{-1} correspond to C=C stretching. A sharp, high-intensity peak at 1128 cm^{-1} is attributed to C–O bending, while peaks observed below 1000 cm^{-1} represent the fingerprint region, which includes complex vibrations such as C–C, C–O, and C–H single bond stretches and bends. The fingerprint region is particularly useful for molecular identification due

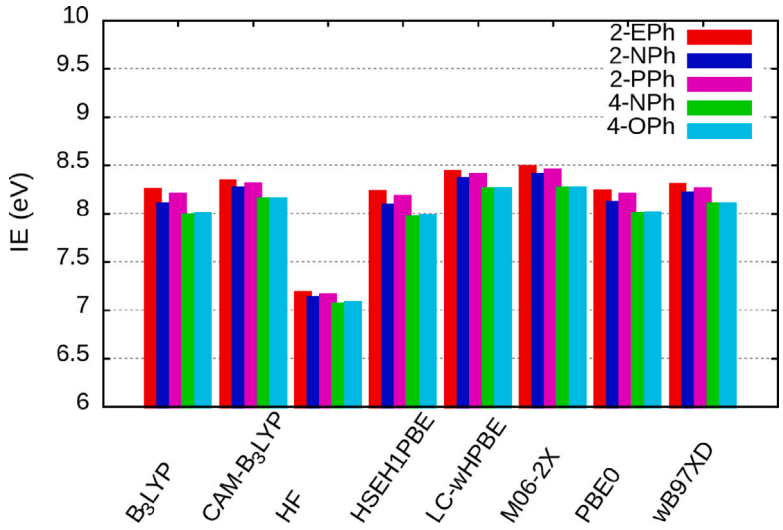

Fig. 2. Ionization energy (IE) of alkylphenols across DFT functional.

Table 2
Computed global reactivity parameters such as chemical potential (μ), chemical hardness (η), softness (σ), electrophilic index (ω), and electronegativity (χ) for alkylphenols occurring in this study. All values are in eV except (σ) which is eV^{-1}.

		2-EPh	2-NPh	2-PPh	4-NPh	4-OPh
B_3LYP	μ	−3.3624	−3.3372	−3.3462	−3.3070	−3.3075
	η	2.8810	2.8869	2.8882	2.8101	2.8101
	σ	0.1736	0.1732	0.1731	0.1779	0.1779
	ω	1.9621	1.9289	1.9384	1.9459	1.9465
	χ	3.3624	3.3372	3.3462	3.3070	3.3075
CAM-B_3LYP	μ	−3.6901	−3.6805	−3.6839	−3.6048	−3.6051
	η	3.9731	3.9643	3.9707	3.9153	3.9156
	σ	0.1258	0.1261	0.1259	0.1277	0.1277
	ω	1.7136	1.7085	1.7089	1.6595	1.6596
	χ	3.6901	3.6805	3.6839	3.6048	3.6051
HF	μ	−3.7278	−3.7198	−3.7229	−3.6529	−3.6533
	η	4.7371	4.7247	4.7336	4.6621	4.6625
	σ	0.1055	0.1058	0.1056	0.1072	0.1072
	ω	1.4668	1.4643	1.4640	1.4310	1.4312
	χ	3.7278	3.7198	3.7229	3.6529	3.6533
HSEH1PBE	μ	−3.3280	−3.3085	−3.3165	−3.2829	−3.2835
	η	2.7127	2.7142	2.7157	2.6296	2.6296
	σ	0.1843	0.1842	0.1841	0.1901	0.1901
	ω	2.0414	2.0165	2.0251	2.0493	2.0500
	χ	3.3280	3.3085	3.3165	3.2829	3.2835
LC-wHPBE	μ	−3.9876	−3.9802	−3.9821	−3.9071	−3.9074
	η	4.9185	4.9065	4.9149	4.8435	4.8438
	σ	0.1017	0.1019	0.1017	0.1032	0.1032
	ω	1.6164	1.6144	1.6132	1.5759	1.5760
	χ	3.9876	3.9802	3.9821	3.9071	3.9074
M06-2X	μ	−3.8688	−3.8639	−3.8643	−3.7886	−3.7886
	η	3.7028	3.6876	3.6980	3.6376	3.6382
	σ	0.1350	0.1356	0.1352	0.1375	0.1374
	ω	2.0211	2.0243	2.0190	1.9730	1.9727
	χ	3.8688	3.8639	3.8643	3.7886	3.7886
PBE0	μ	−3.3394	−3.3169	−3.2843	−3.2871	−3.2875
	η	3.0907	3.0946	3.1371	3.0128	3.0130
	σ	0.1618	0.1616	0.1594	0.1660	0.1659
	ω	1.8041	1.7776	1.7192	1.7932	1.7936
	χ	3.3394	3.3169	3.2843	3.2871	3.2875
wB97XD	μ	−3.5882	−3.5805	−3.5820	−3.5101	−3.5104
	η	4.5970	4.5868	4.5948	4.5308	4.5311
	σ	0.1088	0.1090	0.1088	0.1104	0.1103
	ω	1.4004	1.3975	1.3962	1.3597	1.3598
	χ	3.5882	3.5805	3.5820	3.5101	3.5104

to its unique vibrational patterns. The IR spectra obtained through DFT aligned with the experimental spectra for 2-EPh [54,55].

Table 3
DFT computed oscillator strength (f), excitation energy (E_{Exc}), absorption wavelength (λ_{Max}), electronic transitions, and transition contribution for 2-EPh.

Method	Oscillator strength (f)	2-EPh E_{Exc} (eV)	λ_{Max} (nm)	Major transitions	% Share
B_3LYP	0.4696	6.6346	186.88	HOMO-1→LUMO+4	29
	0.0399	4.9876	248.59	HOMO→LUMO	81
CAM-B_3LYP	0.3354	6.7593	183.43	HOMO-1→LUMO+3	18
	0.0450	5.1990	238.48	HOMO→LUMO+3	49
HF	0.5156	7.2873	170.14	HOMO-1→LUMO+10	35
	0.0598	5.7128	217.80	HOMO→LUMO+11	24
HSEH1PBE	0.4006	6.7942	182.48	HOMO-1→LUMO+4	43
	0.0483	5.0999	243.11	HOMO→LUMO	79
LC-wHPBE	0.5970	7.0398	176.12	HOMO-1→LUMO+7	41
	0.0437	5.3189	233.10	HOMO→LUMO+6	42
M06-2X	0.2851	6.7308	184.20	HOMO-1→LUMO+3	34
	0.0002	5.4065	229.32	HOMO→LUMO	85
PBE0	0.3814	6.8127	181.99	HOMO-1→LUMO+4	52
	0.0004	5.3098	233.50	HOMO→LUMO+1	92
wB97XD	0.6492	6.8490	181.02	HOMO-1→LUMO+7	23
	0.0450	5.1979	238.53	HOMO→LUMO+3	52

From Fig. 3, variations in IR intensities and peak positions across different DFT functionals are evident. For instance, B3LYP, HSEH1PBE, M06-2X, PBE0, and wB97XD exhibit high IR intensities for C–O vibrations, with respective intensities of 272, 262, 262, 307, and 292 at 1128 cm^{-1} (for B3LYP) and 1304 cm^{-1} (for the others). In contrast, range-separated functionals such as CAM-B3LYP and LC-wHPBE predict C–O peaks with lower intensities of 151 and 134 at 1304 cm^{-1} and 1312 cm^{-1}, respectively.

Similarly, O–H stretching is weakly recognized by hybrid functionals, as reflected in their IR intensities: 132 for B3LYP at 3840 cm^{-1}, 142 for PBE0 at 3896 cm^{-1}, and 154 for wB97XD at 3920 cm^{-1}. However, CAM-B3LYP and LC-wHPBE predict sharper O–H peaks at 3880 cm^{-1} and 3920 cm^{-1}, respectively. The pronounced O–H peak observed in M06-2X calculations is likely due to its high exact HF exchange contribution (75%). O–H stretching peaks often appear broad due to varying strengths of hydrogen bonding interactions among alcohol molecules, with frequency shifts primarily influenced by hydrogen bonding strength and O–H bond characteristics.

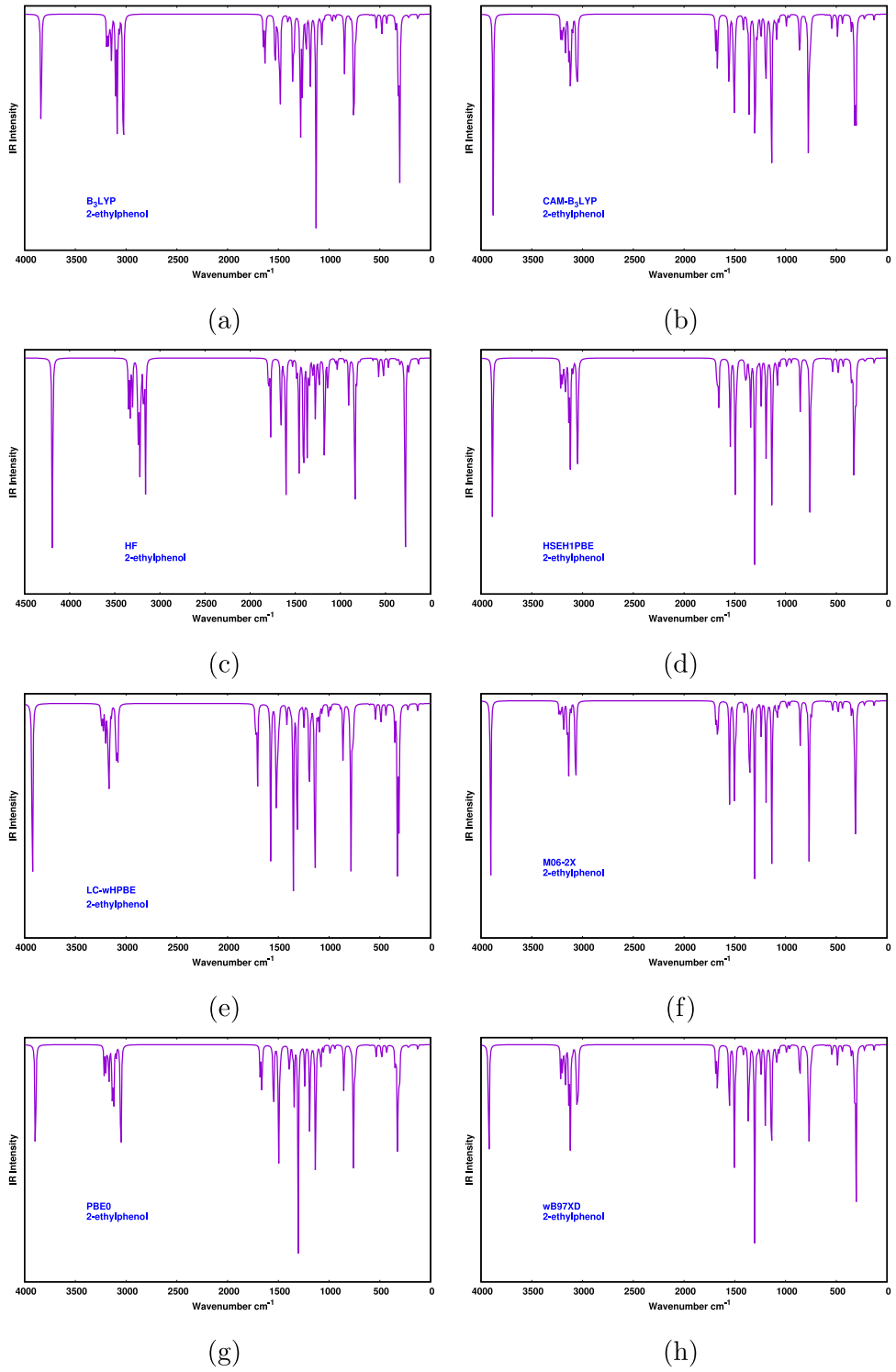

Fig. 3. IR spectra of 2-EPh using various DFT functional combinations with the 6-311++G(d, p) basis set. The spectra illustrate the characteristic vibrational modes of 2-EPh, including O–H stretching, C–H stretching, C–O bending, and other fundamental vibrations. (Broadening parameters: Gaussian, FWHM 4 cm^{-1})

The differences in IR intensities among functionals such as B3LYP, PBE0, M06-2X, CAM-B3LYP, and LC-wHPBE arise from their treatment of electron exchange and correlation effects, particularly in long-range interactions. Functionals like B3LYP, PBE0, and M06-2X, which do not explicitly account for long-range electron correlation effects, tend to overestimate electronic localization and dipole moment derivatives, leading to higher IR intensities. Since IR intensities are proportional to the square of the change in dipole moment during a vibrational transition, these functionals predict enhanced IR signals.

Conversely, CAM-B3LYP and LC-wHPBE incorporate range-separated hybrid exchange, where exact exchange contributions increase with interelectronic distance. This approach mitigates the overestimation of electronic delocalization, leading to more accurate dipole moment derivatives and, consequently, lower IR intensities. By improving the description of long-range interactions, these functionals

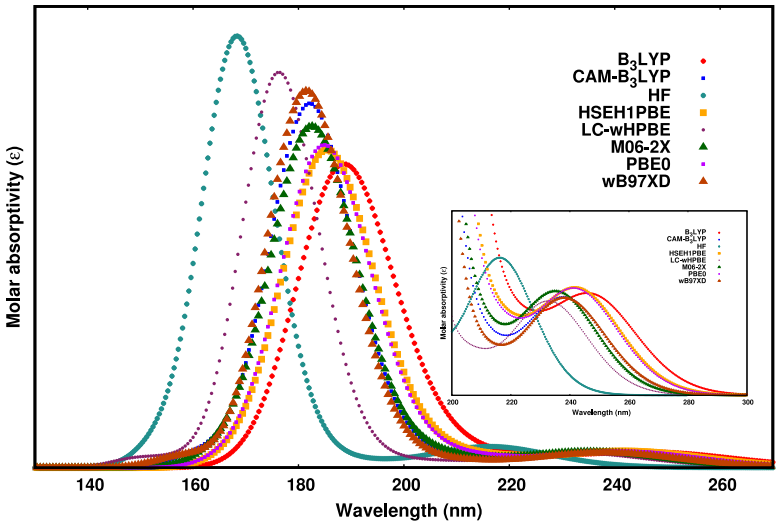

Fig. 4. UV–Vis spectra of 2-EPh across DFT functional. Inset image showing absorption spectra with lower ϵ values but at higher excitation wavelength. (Broadening parameters: UV–Vis peak half width at half height 0.33 eV and Gaussian broadening).

provide more reliable predictions of IR spectral features, especially for molecules exhibiting significant charge delocalization or hydrogen bonding interactions.

3.2.2. Electron spectra

The computed excitation energies, oscillator strengths (f), excitation wavelengths (λ_{Max}), excited-state spectral transitions, and transition occupancies of 2-EPh are summarized in Table 3. The UV–Vis spectra, which contain absorption bands with maximum excitation wavelengths using various DFT functionals are shown in Fig. 4. Excitation energies and corresponding oscillator strengths for 20 singlet excited states were computed to analyze the electronic transitions and absorption characteristics of the system.

For 2-EPh using the B3LYP functional, the primary absorption peak is observed at 186.88 nm having molar absorptivity, ϵ (L mol^{-1} cm^{-1}) = 37 516. Additionally, a secondary absorption band appears at 248.59 nm (ϵ = 1940), though with a lower oscillator strength of 0.0399, as shown in the inset of Fig. 4. The electronic transitions for two excited states, along with their oscillator strengths, excitation energies, wavelengths, and percentage contributions, are summarized in Table 3. B3LYP, which includes 20% exact Fock exchange, lacks the necessary exact HF exchange contribution at both short and long ranges, which is essential for accurately describing excited-state properties. For range-separated functionals, which incorporate exact HF exchange at both short and long ranges, the λ_{Max} values are 183.43 nm (ϵ = 45 008) and 238.48 nm (ϵ = 1868) for CAM-B3LYP and 176.12 nm (ϵ = 48 839) and 233.10 nm (ϵ = 1790) for LC-wHPBE which contains 100% exact HF exchange at long-range. It is important to note that lower λ_{Max} values correspond to the transitions with the highest oscillator strengths. The computed spectra also exhibit absorption at longer λ_{Max}; however, these peaks are associated with lower ϵ values. Among the hybrid functionals, the trend in maximum excitation wavelength λ_{Max} follows the order: B3LYP > M06-2X > HSEH1PBE > PBE0 > wB97XD.

Among the functionals examined, HF produces the highest absorption peak, whereas B3LYP exhibits the lowest. Range-separated functionals like CAM-B3LYP and LC-wHPBE fall between these extremes. Additionally, the values obtained for wB97XD and M06-2X are closer to those of range-separated functionals, likely due to the inclusion of dispersion correction in wB97XD and the high exact HF exchange (54%) in M06-2X.

Regarding the shift in the absorption bands of 2-EPh, aromatic compounds such as benzene exhibit two primary absorption bands at approximately 184 nm (ϵ = 47 000) and 202 nm (ϵ = 7400). In contrast, phenol has a maximum absorption wavelength λ_{Max} of 211 nm, attributed to a π-π^* transition [56]. For 2-EPh, the B3LYP calculations predict an excitation at 186.88 nm corresponding to a π-π^* transition, while the excitation at 245.59 nm is assigned to an n-π^* transition involving promotion of an oxygen lone-pair electron to an antibonding π^* orbital. Substituents at the ortho position of phenol can influence the excitation wavelength through both electronic and steric effects [19].

The ethyl substituent behaves as an electron-donating group via hyperconjugation, donating electron density from the σ(C–H) bonds into the aromatic π framework. Consequently, the electron density in the aromatic ring increases, leading to an elevation of the HOMO (π) level and a relative stabilization of the LUMO, which collectively results in a decrease in the HOMO–LUMO gap ΔE_G. Consequently, the reduced HOMO–LUMO gap produces a bathochromic (red) shift, shifting the absorption maximum to longer wavelengths. The obtained results have shown a bathochromic shift in the excitation wavelength λ_{Max} for different functional following the theoretical explanation.

Additionally, steric effects may also play a role, though they are typically minor compared to electronic effects in influencing the absorption characteristics. Similar trends are observed across different DFT functionals, each predicting varying transition energies, wavelengths, and major contributions to the excitation process, demonstrating their influence on electronic structure calculations. A comprehensive visualization of the variation of wavelengths across different DFT functional for investigated molecules is shown in Fig. 5. Table 3 highlights the excited states with the maximum excitation wavelength, comprising major transition contribution and their respective percentage occupancies. For B3LYP, the dominant transition is from HOMO-1 to LUMO+4, with the highest occupancy of 29%. A total of ten transitions contribute to the absorption spectrum, each with individual contributions, however, very small. The secondary absorption band (typical for phenolic compounds) with B3LYP at 248.59 nm along with transition contribution 81% is also shown. Similarly, for CAM-B3LYP, there are three major transitions with contributions of 18%, 16%, and 15%, respectively. Again, there are 10 such transitions comprising excited state of CAM-B3LYP in primary absorption band. A similar pattern can be observed in calculations using other DFT functionals for primary and secondary absorption bands.

3.3. Chemical ionization mass spectrometry

Both PTR-MS and SIFT-MS are soft chemical ionization, real-time MS techniques excellent for volatile and semi-volatile organics. PTR-MS

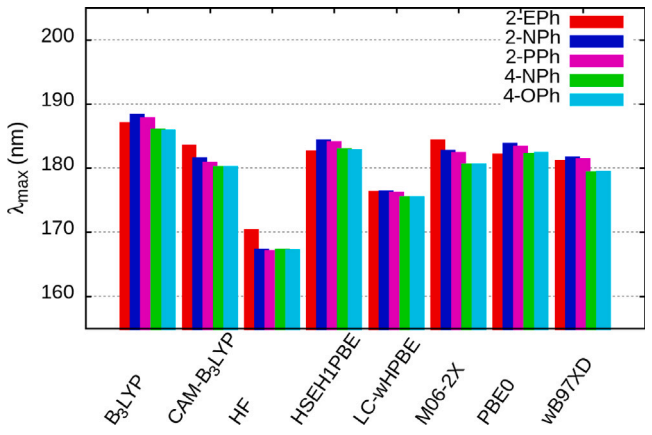

Fig. 5. Maximum excitation wavelength (λ_{Max}) of alkylphenols under study across DFT functional.

Table 4
Evaluated enthalpy change (ΔH) and Gibbs free energy (ΔG) of charge transfer and hydride (H^-) abstraction reaction between NO^+ and alkylphenols using B3LYP/6-311++g(d, p) DFT method at 298.15 K.

NO^+ Reactions	ΔH (KCal/mol)	ΔG (KCal/mol)
Charge transfer reactions		
$NO^+ + C_8H_{10}O$ (2-EPh) → $C_8H_{10}O^+ + NO$	−40.76	−41.85
$NO^+ + C_{15}H_{24}O$ (2-NPh) → $C_{15}H_{24}O^+ + NO$	−44.12	−45.25
$NO^+ + C_9H_{12}O$ (2-PPh) → $C_9H_{12}O^+ + NO$	−41.86	−42.95
$NO^+ + C_{15}H_{24}O$ (4-NPh) → $C_{15}H_{24}O^+ + NO$	−46.90	−47.65
$NO^+ + C_{14}H_{22}O$ (4-OPh) → $C_{14}H_{22}O^+ + NO$	−46.67	−47.45
Hydride (H^-) abstraction		
$NO^+ + C_8H_{10}O$ (2-EPh) → $C_8H_9O^+ + HNO$	+62.59	+61.71
$NO^+ + C_{15}H_{24}O$ (2-NPh) → $C_{15}H_{23}O^+ + HNO$	+57.67	+56.52
$NO^+ + C_9H_{12}O$ (2-PPh) → $C_9H_{11}O^+ + HNO$	+60.71	+59.86
$NO^+ + C_{15}H_{24}O$ (4-NPh) → $C_{15}H_{23}O^+ + HNO$	+55.45	+55.14
$NO^+ + C_{14}H_{22}O$ (4-OPh) → $C_{14}H_{21}O^+ + HNO$	+55.66	+55.33

and SIFT-MS provide high time resolution, direct gas-phase analysis, and (for SIFT-MS) robust quantitation via known ion–molecule kinetics with selectable reagent ions (H_3O^+, NO^+, O_2^+). They excel in VOCs and breath/air monitoring. Proton transfer reaction (PTR) relies on proton transfer — only molecules with proton affinity above water will react efficiently. However, charge transfer reactions via NO^+, O_2^+ are frequently studied in case the proton affinity of molecules is below that of water, reactions via PTR occur through fragmentation or the VOC under study is not detectable through PTR [57–59]. SIFT-MS advantage includes multiple reagent ions, and kinetic databases can facilitate quantitation when reaction rate constants are known or can be measured/estimated. However, switchable reagent ion mass spectrometry (SRI-MS) is a proprietary technology of PTR-MS, where the user can select from different reagent ions for chemical ionization direct injection mass spectrometry. Through fast switching of the reagent ions (less than 10 s) different reaction pathways can be triggered. Still, method validation (calibration, matrix effects, recovery) is essential.

3.3.1. NO^+-CIMS ion chemistry

In PTR-MS, reagent ions are most commonly H_3O^+, but alternative reagent ions such as NO^+ can also be employed in CIMS mode to extend selectivity [60].

Ionization mechanism of NO^+ includes with analyte molecules primarily through charge transfer (5), hydride (H^-) abstraction (6), and association (7). Charge transfer:

$$NO^+ + M \rightarrow M^+ + NO \quad (5)$$

$$NO^+ + MH \rightarrow M^+ + HNO \quad (6)$$

$$NO^+ + M \rightarrow M.NO^+ \quad (7)$$

Charge transfer takes place when the IE of the analyte (M) is lower than that of NO (9.26 eV), whereas association reactions are generally favored for aromatic species and highly polarizable molecules. The ionization energies of all alkylphenols considered in this study are well below the IE of NO, indicating their suitability for charge transfer. The enthalpy changes (ΔH) and Gibbs free energy (ΔG) for charge transfer and hydride abstraction reactions of NO^+ with the major alkylphenols were computed and are presented in Table 4. The results show that charge transfer is exothermic and therefore a favorable pathway, while hydride abstraction is endothermic and unlikely to occur under PTR-MS conditions with NO^+ reagent ions. Similarly, the association of alkylphenols with NO^+ was found to be unfavorable. Overall, the data indicate that charge transfer reactions proceed at the collisional limit, occurring upon nearly every encounter, and the corresponding rate constants are calculated in Section 3.3.2.

NO^+ reagent ions provide a broader ionization range, allowing detection of VOCs that do not react efficiently with H_3O^+ (e.g., certain hydrocarbons, aldehydes, aromatics). Also, isomer differentiation is another advantage. Different VOCs can show distinct fragmentation or adduct patterns with NO^+, improving selectivity. Reduced water clustering compared to H_3O^+, which can simplify spectra.

3.3.2. CIMS reaction collision rates

The absolute quantification of VOCs relies on the kinetics of ion–molecule reactions between reagent ions (e.g., H_3O^+, NO^+, O_2^+) and analyte molecules [57,58]. The signal intensity measured is directly proportional to the product ion concentration, which depends on the reaction rate constant (k), the reagent ion concentration, and the reaction time within the drift tube or flow tube. In PTR-MS, absolute quantification often assumes that reactions proceed at the collisional (Langevin) limit [61]; however, deviations occur, making accurate rate constants important for compounds with atypical proton affinities. If the rate constant is underestimated or overestimated, the calculated VOC concentration will be correspondingly biased.

In CIMS, ion–molecule reaction rates are governed by long-range electrostatic capture, with the Langevin model (ion–induced dipole) giving a baseline rate constant, and the Su–Chesnavich [62] correction accounting for permanent dipole orientation, linking polarizability and dipole moment of neutrals to experimentally observed kinetics. A point charge (ion) induces a dipole moment in a neutral molecule of polarizability (α). According to classical capture theory, the rate constant is given by

$$k_{Lang} = \sqrt{\frac{\pi \alpha q^2}{\mu \epsilon_0}}, \quad (8)$$

where $q = z\,q_e$ is the charge of the ion (q_e is the elementary charge in Coulomb); α is the polarizability of the neutral species, μ is the reduced mass of the reactants, and ϵ_0 is the permittivity of free space. Since capture probability is governed by long-range forces, k_{Lang} is independent of temperature. Typical value of k_{Lang} expected as 10^{-9} cm^3 s^{-1}.

If the neutral has a permanent dipole moment (μ_D), the interaction is stronger and orientation-dependent. The rate constants of such ion–molecule reactions are given by the method provided by Su and Chesnavich. According to which a classical trajectory models an ion as a point charge and the polar molecule as a two-dimensional rigid rotor via the following parameterized equations:

$$k_{cap} = k_{Lang}\, K_c(\tau, \epsilon), \quad (9)$$

where K_c is the ion–molecule capture-rate coefficient at a given center-of-mass kinetic energy ($K E_{com}$) by reduced parameters τ and ϵ as given

Table 5
Computed rate coefficients k_{Lang} [61] and k_{cap} [62] for the charge transfer reaction of NO^+ with alkylphenols, in the units of (10^{-9} cm^3 s^{-1}) at different reduced electric field values. PTR-MS drift tube conditions (T = 300–480 K), E/N = 100–150 Td (where E/N is the ratio of electric field to gas number density and Td = Townsend = 10^{-21} $V m^2$).

Molecule	T		NO^+ k_{cap}(10^{-9} cm^3 s^{-1})					
	K	E/N →	100	110	120	130	140	150
2-EPh	300	k_{Lang} = 1.81	1.93	1.91	1.90	1.89	1.88	1.87
	350		1.92	1.91	1.89	1.88	1.87	1.87
	400		1.91	1.90	1.89	1.88	1.87	1.86
	480		1.91	1.89	1.88	1.87	1.87	1.86
2-NPh	300	k_{Lang} = 2.39	2.47	2.46	2.45	2.44	2.44	2.43
	350		2.46	2.45	2.45	2.44	2.43	2.43
	400		2.46	2.45	2.44	2.44	2.43	2.43
	480		2.45	2.45	2.44	2.43	2.43	2.42
2-PPh	300	k_{Lang} = 1.91	2.02	2.01	1.99	1.98	1.97	1.97
	350		2.02	2.00	1.99	1.98	1.97	1.96
	400		2.01	2.00	1.98	1.97	1.97	1.96
	480		2.00	1.99	1.98	1.97	1.96	1.96
4-NPh	300	k_{Lang} = 2.40	2.53	2.51	2.49	2.48	2.47	2.46
	350		2.52	2.50	2.49	2.48	2.47	2.46
	400		2.51	2.50	2.48	2.47	2.46	2.46
	480		2.50	2.49	2.48	2.47	2.46	2.45
4-OPh	300	k_{Lang} = 2.32	2.46	2.44	2.43	2.41	2.40	2.39
	350		2.46	2.44	2.42	2.41	2.40	2.39
	400		2.45	2.43	2.42	2.41	2.40	2.39
	480		2.44	2.42	2.41	2.40	2.39	2.38

below.

$$\tau = \frac{\mu_D}{\sqrt{\alpha T}}, \tag{10}$$

and

$$\epsilon = \frac{\mu_D}{\sqrt{\alpha K E_{com}}}. \tag{11}$$

For more information, refer to the related literature [62–64]. The obtained results are given in Table 5, where the rate constants for charge transfer reaction between NO^+ and alkylphenols are reported at varying reduced electric field at different elevated temperatures as occur under PTR-MS highly energetic conditions. In a typical SRI-MS instrument [65,66] (switchable reagent ion version of PTR-MS), the E/N value can vary from 80 to 155 Td (where 1 Td = 1 Townsend = 10^{-17} $V cm^2$), a range covered in the present calculations. Table 5 lists the computed reaction rates for charge transfer from NO^+ ions in SRI-MS under the following conditions: E/N = 100–150 Td, air as buffer gas (averaged over N_2 and O_2), and T = 300 K to 480 K.

It is observed that increasing the temperature leads to a decrease in reaction rate constants, consistent with theoretical expectations and numerous experimental findings. Similarly, higher E/N values (electric field to gas number density ratio) result in reduced rate constants, although the relative decrease becomes less pronounced at elevated E/N. The anticipated rates thus diminish with increasing E/N or center-of-mass kinetic energy. Within a PTR/SRI-MS drift tube, the kinetics are governed not only by pressure and temperature but also by the applied electric field. This field imparts additional energy to collisions, making them significantly more energetic (typically 0.1–0.5 eV) than thermal collisions occurring at room temperature.

4. Conclusions

DFT calculations were performed to investigate the structural, electronic, chemical reactivity, and optical properties of alkylphenols. A comprehensive benchmark study was conducted to evaluate the accuracy in predicting electronic and UV–Vis properties. The results indicate that hybrid functionals such as B3LYP and PBE0 are well-suited for ground-state calculations, providing IE values that closely align with experimental data. Further, B3LYP/6-311++G(d, p) DFT method computed dipole moment and polarizability, is selected for the calculation of rate constants for NO^+-alkylphenol reactions.

The computed IE values using B3LYP, HSEH1PBE, PBE0, and wB97XD demonstrate strong agreement with reported values, highlighting the role of 20%–25% exact HF exchange in improving prediction accuracy. Global reactivity calculations further reveal that range-separated functionals such as CAM-B3LYP, wB97XD, and LC-wHPBE, as well as the hybrid functional M06-2X, show a strong correlation with the Koopmans approximation (IE ≈ $-\epsilon_{HOMO}$), while B3LYP, PBE0, and HSEH1PBE better correlate with electron affinity (EA ≈ $-\epsilon_{LUMO}$). For vibrational properties, functionals like B3LYP, PBE0, and M06-2X tend to overestimate electronic localization and dipole moment derivatives, leading to higher IR intensities. In contrast, range-separated functionals such as CAM-B3LYP and LC-wHPBE provide more accurate dipole moment derivatives by mitigating overestimation of electronic delocalization, resulting in lower IR intensities.

The UV–Vis spectra computed from range-separated functionals (CAM-B3LYP and LC-wHPBE) exhibit intermediate absorption values between the extremes of HF and B3LYP. Functionals such as wB97XD and M06-2X show absorption characteristics similar to range-separated functionals, which can be attributed to dispersion corrections in wB97XD and the high exact HF exchange (54%) in M06-2X.

The computed reaction enthalpies (Δ*H*) and Gibbs free energy (Δ*G*) analysis indicate that NO^+ readily undergoes charge transfer with alkylphenols. This charge transfer process is exothermic and proceeds at collision-controlled rates. In contrast, hydride abstraction by NO^+ is endothermic, while the association pathway is not favorable. These results highlight the effectiveness of NO^+ as a reagent ion for the detection and quantification of alkylphenols in CIMS techniques such as PTR-MS and SIFT-MS.

This study provides a fundamental molecular-level understanding of alkylphenols through the analysis of their electronic properties and chemical reactivity parameters. The IR and UV–Vis investigations yield validated spectroscopic fingerprints for molecular identification and conformational analysis. In addition, the study offers mechanistic insights into CI-MS detection and ion–molecule chemistry relevant to alkylphenols and other structurally related compounds of environmental and health concern.

Declaration of competing interest

The author declares no conflict of interest.

Appendix A. Supplementary data

Optimized structure coordinates using B3LYP/6-311++g(d, p) DFT method of alkylphenols are provided (S1), along with excited state spectra (S2), collected as supplementary materials.

Supplementary material related to this article can be found online at https://doi.org/10.1016/j.comptc.2026.115682.

Data availability

Data will be made available on request.

References

[1] G. Bhandari, A.R. Bagheri, P. Bhatt, M. Bilal, Occurrence, potential ecological risks, and degradation of endocrine disrupter, nonylphenol, from the aqueous environment, Chemosphere 275 (2021) 130013.

[2] S.I. Kaya, A. Cetinkaya, N.K. Bakirhan, S.A. Ozkan, Trends in sensitive electrochemical sensors for endocrine disruptive compounds, Trends Environ. Anal. Chem. 28 (2020) e00106.

[3] X. Xu, X. Wang, X. Li, Q. Liu, A theoretical study on the photodegradation mechanism of the endocrine disrupting chemical p-nonylphenol induced by OH in water, Marine Poll. Bull. 173 (2021) 113107.

[4] C. Groshart, Chemical Study on Alkylphenols, RIKZ, 2001.

[5] J. Yang, Q. Huang, H. Liu, X. Zhou, Z. Huang, Q. Peng, C. Liu, 4-Nonylphenol and 4-tert-octylphenol induce anxiety-related behaviors through alternation of 5-HT receptors and transporters in the prefrontal cortex, Comp. Biochem. Physiol. C 230 (2020) 108701.

[6] A.M. Romanelli, A. Montefusco, S. Sposito, B. Scafuri, I. Caputo, G. Paolella, In vitro investigation of biological and toxic effects of 4-octylphenol on human cells, Int. J. Mol. Sci. 25 (23) (2024).

[7] S. Senthil Kumaran, C. Kavitha, M. Ramesh, T. Grummt, Toxicity studies of nonylphenol and octylphenol: Hormonal, hematological and biochemical effects in clarias gariepinus, J. Appl. Toxicol. 31 (8) (2011) 752–761.

[8] A.R. Fernandes, C.T. Costley, M. Rose, Determination of 4-octylphenol and 4-nonylphenol congeners in composite foods, Food Addit. Contam. 20 (9) (2003) 846–852.

[9] A. Galazka, U. Jankiewicz, Endocrine disrupting compounds (nonylphenol and bisphenol a)-sources, harmfulness and laccase-assisted degradation in the aquatic environment, Microorganisms 10 (11) (2022).

[10] D. Smith, P. Španěl, Direct, rapid quantitative analyses of BVOCs using SIFT-MS and PTR-MS obviating sample collection, TRAC Trends Anal. Chem. 30 (7) (2011) 945–959, Biogenic Volatile Organic Compounds S.I..

[11] A.J. Taylor, J.D. Beauchamp, V.S. Langford, Non-destructive and high-throughput—APCI-MS, PTR-MS and SIFT-MS as methods of choice for exploring flavor release, in: Dynamic Flavor: Capturing Aroma using Real-Time Mass Spectrometry, pp. 1–16, Chapter 1.

[12] L. Padmaja, C. Ravikumar, D. Sajan, I. Hubert Joe, V.S. Jayakumar, G.R. Pettit, O. Faurskov Nielsen, Density functional study on the structural conformations and intramolecular charge transfer from the vibrational spectra of the anticancer drug combretastatin-A2, J. Raman Spectrosc. 40 (4) (2009) 419–428.

[13] V. Dixit, R. Yadav, DFT-B3LYP computations of electro and thermo molecular characteristics and mode of action of fungicides (chlorophenols), Int. J. Pharm. 491 (1) (2015) 277–284.

[14] M. Bhatia, An overview of conceptual-DFT based insights into global chemical reactivity of volatile sulfur compounds (VSCs), Comput. Toxicol. 29 (2024) 100295.

[15] M. Pernica, P. Poloucká, M. Seifertová, Z. Šimek, Determination of alkylphenols in water samples using liquid chromatography–tandem mass spectrometry after pre-column derivatization with dansyl chloride, J. Chromatogr. A 1417 (2015) 49–56.

[16] M. Oppegård, B.H. Hansen, L. Sørensen, Determination of C0–C9 alkyl phenols in produced-water-exposed fish eggs using gas chromatography/tandem mass spectrometry, Rapid Commun. Mass Spectrom. 34 (24) (2020) e8950, e8950 RCM-20-0269.R1.

[17] Z. Kuklenyik, J. Ekong, C.D. Cutchins, L.L. Needham, A.M. Calafat, Simultaneous measurement of urinary bisphenol a and alkylphenols by automated solid-phase extractive derivatization gas chromatography/mass spectrometry, Anal. Chem. 75 (24) (2003) 6820–6825.

[18] G. Zhang, N. Li, Y. Zhang, J. Pan, D. Gong, Binding mechanism of 4-octylphenol with human serum albumin: Spectroscopic investigations, molecular docking and dynamics simulation, Spectrochim. Acta A 255 (2021) 119662.

[19] S. Tetteh, R. Zugle, J.P.K. Adotey, A. Quashie, Electronic spectra of ortho-substituted phenols: An experimental and DFT study, J. Spectrosc. 2018 (1) (2018) 4193657.

[20] M. Štekláč, M. Breza, DFT studies of the toxicity of alkylphenols to tetrahymena pyriformis, Polyhedron 207 (2021) 115360.

[21] M. Sugimoto, A.B. Manggara, K. Yoshida, T. Inoue, T. Ideo, An electronic-structure informatics study on the toxicity of alkylphenols to tetrahymena pyriformis, Mol. Inform. 39 (1–2) (2020) 1900121.

[22] S. bin Jo, M. Ahn, K. Bhattarai, K.-R. Wee, D.-H. Ahn, J.-W. Song, UV/Vis absorption spectrum calculations of benzo-1,2-dipyrene isomer using long-range corrected density functional theory, Chem. Phys. Lett. 761 (2020) 138023.

[23] M. Van Bay, N.K. Hien, P.T.D. Tran, N.T.K. Tuyen, D.T.Y. Oanh, P.C. Nam, D.T. Quang, TD-DFT benchmark for UV-vis spectra of coumarin derivatives, Vietnam. J. Chem. 59 (2) (2021) 203–210.

[24] K. Batra, S. Zahn, T. Heine, Benchmark of simplified time-dependent density functional theory for UV–Vis spectral properties of porphyrinoids, Adv. Theory Simul. 3 (1) (2020) 1900192.

[25] M.J. Frisch, G.W. Trucks, H.B. Schlegel, G.E. Scuseria, M.A. Robb, J.R. Cheeseman, G. Scalmani, V. Barone, G.A. Petersson, H. Nakatsuji, X. Li, M. Caricato, A.V. Marenich, J. Bloino, B.G. Janesko, R. Gomperts, B. Mennucci, H.P. Hratchian, J.V. Ortiz, A.F. Izmaylov, J.L. Sonnenberg, D. Williams-Young, F. Ding, F. Lipparini, F. Egidi, J. Goings, B. Peng, A. Petrone, T. Henderson, D. Ranasinghe, V.G. Zakrzewski, J. Gao, N. Rega, G. Zheng, W. Liang, M. Hada, M. Ehara, K. Toyota, R. Fukuda, J. Hasegawa, M. Ishida, T. Nakajima, Y. Honda, O. Kitao, H. Nakai, T. Vreven, K. Throssell, J.A. Montgomery, J.E. Peralta, F. Ogliaro, M.J. Bearpark, J.J. Heyd, E.N. Brothers, K.N. Kudin, V.N. Staroverov, T.A. Keith, R. Kobayashi, J. Normand, K. Raghavachari, A.P. Rendell, J.C. Burant, S.S. Iyengar, J. Tomasi, M. Cossi, J.M. Millam, M. Klene, C. Adamo, R. Cammi, J.W. Ochterski, R.L. Martin, K. Morokuma, O. Farkas, J.B. Foresman, D.J. Fox, Gaussian 16 revision C.01, 2016, Gaussian Inc. Wallingford CT.

[26] M.E. Casida, C. Jamorski, K.C. Casida, D.R. Salahub, Molecular excitation energies to high-lying bound states from time-dependent density-functional response theory: Characterization and correction of the time-dependent local density approximation ionization threshold, J. Chem. Phys. 108 (11) (1998) 4439–4449.

[27] R. Bauernschmitt, R. Ahlrichs, Treatment of electronic excitations within the adiabatic approximation of time dependent density functional theory, Chem. Phys. Lett. 256 (4) (1996) 454–464.

[28] E. Gross, W. Kohn, Time-dependent density-functional theory, in: P.-O. Löwdin (Ed.), Density Functional Theory of Many-Fermion Systems, in: Advances in Quantum Chemistry, vol. 21, Academic Press, 1990, pp. 255–291.

[29] C. Ullrich, Z.-h. Yang, A brief compendium of time-dependent density functional theory, Braz. J. Phys. 44 (2013).

[30] T. Koopmans, Ordering of wave functions and eigenvalues to the individual electrons of an atom, Physica 1 (1) (1934) 104–110.

[31] A. Toro-Labbé, in: A. Toro-Labbé (Ed.), Theoretical Aspects of Chemical Reactivity, first ed., vol. 19, Elsevier Science, UK, 2007, pp. 19–33, Chapter 2-3.

[32] R.G. Pearson, Absolute electronegativity and hardness correlated with molecular orbital theory, Proc. Natl. Acad. Sci. 83 (22) (1989) 8440–8441.

[33] F. Jensen, Introduction To Computational Chemistry, Wiley, 2017.

[34] K. Ramirez-Balderrama, E. Orrantia-Borunda, N. Flores-Holguin, Calculation of global and local reactivity descriptors of carbodiimides, a DFT study, J. Theor. Comput. Chem. 16 (03) (2017) 1750019.

[35] C. Lee, W. Yang, R.G. Parr, Development of the Colle-Salvetti correlation-energy formula into a functional of the electron density, Phys. Rev. B 37 (2) (1988) 211–212.

[36] C. Adamo, V. Barone, Toward reliable density functional methods without adjustable parameters: The PBE0 model, J. Chem. Phys. 110 (13) (1999) 6158–6170.

[37] Y. Zhao, D. Truhlar, The M06 suite of density functionals for main group thermochemistry, thermochemical kinetics, noncovalent interactions, excited states, and transition elements: Two new functionals and systematic testing of four M06 functionals and 12 other functionals, Theor. Chem. Accounts 120 (2008) 215–241.

[38] T. Yanai, D.P. Tew, N.C. Handy, A new hybrid exchange–correlation functional using the Coulomb-attenuating method (CAM-B3LYP), Chem. Phys. Lett. 393 (1) (2004) 51–57.

[39] T.M. Henderson, A.F. Izmaylov, G. Scalmani, G.E. Scuseria, Can short-range hybrids describe long-range-dependent properties? J. Chem. Phys. 131 (4) (2009) 044108.

[40] J.-w. Song, T. Hirosawa, T. Tsuneda, K. Hirao, Long-range corrected density functional calculations of chemical reactions: Redetermination of parameter, J. Chem. Phys. 126 (2007) 154105.

[41] K. Okuno, Y. Shigeta, R. Kishi, H. Miyasaka, M. Nakano, Tuned CAM-B3LYP functional in the time-dependent density functional theory scheme for excitation energies and properties of diarylethene derivatives, J. Photochem. Photobiol. A 235 (2012) 29–34.

[42] J. Heyd, G.E. Scuseria, Efficient hybrid density functional calculations in solids: Assessment of the Heyd–Scuseria–Ernzerhof screened Coulomb hybrid functional, J. Chem. Phys. 121 (3) (2004) 1187–1192.

[43] J. Heyd, G.E. Scuseria, M. Ernzerhof, Erratum: "Hybrid functionals based on a screened Coulomb potential" [J. Chem. Phys. 118, 8207 (2003)], J. Chem. Phys. 124 (21) (2006) 219906.

[44] J. Heyd, J.E. Peralta, G.E. Scuseria, R.L. Martin, Energy band gaps and lattice parameters evaluated with the Heyd-Scuseria-Ernzerhof screened hybrid functional, J. Chem. Phys. 123 (17) (2005) 174101.

[45] J.-D. Chai, M. Head-Gordon, Long-range corrected hybrid density functionals with damped atom–atom dispersion corrections, Phys. Chem. Chem. Phys. 10 (2008) 6615–6620.

[46] A.D. McLean, G.S. Chandler, Contracted Gaussian basis sets for molecular calculations. I. Second row atoms, Z=11–18, J. Chem. Phys. 72 (10) (1980) 5639–5648.

[47] R. Krishnan, J.S. Binkley, R. Seeger, J.A. Pople, Self-consistent molecular orbital methods. XX. A basis set for correlated wave functions, J. Chem. Phys. 72 (1) (1980) 650–654.

[48] T. Clark, J. Chandrasekhar, G.W. Spitznagel, P.V.R. Schleyer, Efficient diffuse function-augmented basis sets for anion calculations. III. The 3-21+G basis set for first-row elements, Li–F, J. Comput. Chem. 4 (3) (1983) 294–301.

[49] M.J. Frisch, J.A. Pople, J.S. Binkley, Self-consistent molecular orbital methods 25. Supplementary functions for Gaussian basis sets, J. Chem. Phys. 80 (7) (1984) 3265–3269.
[50] A. Shukla, R. Tewari, G. Khan, Study of phenol and its derivatives based on dipole moment, J. Chem. Pharm. Res. 3 (2011) 79–83.
[51] R. Stenutz, 4-Octylphenol, 2025, https://www.stenutz.eu/chem/solv6%20(2).php?name=4-octylphenol. (Accessed 01 February 2025).
[52] J.L. Lin, K.C. Lin, W.B. Tzeng, Mass-analyzed threshold ionization spectroscopy of o-, m-, and p- methylaniline cations: Vicinal substitution effects on electronic transition, ionization, and molecular vibration, J. Phys. Chem. A 106 (27) (2002) 6462–6468.
[53] S.K. Kim, S.C. Hsu, S. Li, E.R. Bernstein, Excited state proton transfer in the S1 state of 2-allylphenol, 2-propenylphenol, and 2-propylphenol and their van der waals clusters with water and ammonia, J. Chem. Phys. 95 (5) (1991) 3290–3301.
[54] ChemicalBook, 2-ethylphenol(90-00-6) IR1, 2025, URL https://www.chemicalbook.com/SpectrumEN_90-00-6_IR1.htm. (Accessed 01 February 2025).
[55] NIST, Database for IR spectra of 2-ethylphenol, 2025, URL https://webbook.nist.gov/cgi/cbook.cgi?ID=C90006&Mask=80. (Accessed 01 February 2025).
[56] R. Pratiwi, A. Nandiyanto, How to read and interpret UV-VIS spectrophotometric results in determining the structure of chemical compounds, Indones. J. Educ. Res. Technol. 2 (2022) 1–20.
[57] A.R. Koss, C. Warneke, B. Yuan, M.M. Coggon, P.R. Veres, J.A. de Gouw, Evaluation of NO^+ reagent ion chemistry for online measurements of atmospheric volatile organic compounds, Atmos. Meas. Tech. 9 (7) (2016) 2909–2925.
[58] P. Španěl, A. Spesyvyi, D. Smith, Electrostatic switching and selection of H3O+, NO+, and O2+• reagent ions for selected ion flow-drift tube mass spectrometric analyses of air and breath, Anal. Chem. 91 (8) (2019) 5380–5388.
[59] M. Bhatia, N. Manini, F. Biasioli, L. Cappellin, Theoretical investigation of charge transfer from NO+ and O2+ ions to wine-related volatile compounds for mass spectrometry, J. Am. Soc. Mass Spectrom. 33 (2) (2022) 251–264, PMID: 35020398.
[60] A.M. Ellis, C.A. Mayhew, Proton Transfer Reaction Mass Spectrometry Principles and Applications, John Wiley & Sons, Chichester, United Kingdom, 2014.
[61] P. Langevin, A fundamental formula for kinetic theory, Ann. Chim. Phys. 5 (245) (1905).
[62] T. Su, Parametrization of kinetic energy dependences of ion-polar molecule collision rate constants by trajectory calculations, J. Chem. Phys. 100 (6) (1994) 4703–4703.
[63] T. Su, W.J. Chesnavich, Parametrization of the ion-polar molecule collision rate constant by trajectory calculations, J. Chem. Phys. 76 (10) (1982) 5183–5185.
[64] T. Su, Trajectory calculations of ion-polar molecule capture rate constants at low temperatures, J. Chem. Phys. 88 (6) (1988) 4102–4103.
[65] P. Sulzer, A. Edtbauer, E. Hartungen, S. Jürschik, A. Jordan, G. Hanel, S. Feil, S. Jaksch, L. Märk, T.D. Märk, From conventional proton-transfer-reaction mass spectrometry (PTR-MS) to universal trace gas analysis, Int. J. Mass Spectrom. 321–322 (2012) 66–70.
[66] A. Jordan, S. Haidacher, G. Hanel, E. Hartungen, J. Herbig, L. Märk, R. Schottkowsky, H. Seehauser, P. Sulzer, T. Märk, An online ultra-high sensitivity proton-transfer-reaction mass-spectrometer combined with switchable reagent ion capability PTR+SRI-MS, Int. J. Mass Spectrom. 286 (1) (2009) 32–38.